

# SCIENTIFIC REPORTS

OPEN

## Effects of local structure of $\text{Ce}^{3+}$ ions on luminescent properties of $\text{Y}_3\text{Al}_5\text{O}_{12}:\text{Ce}$ nanoparticles

Xiaowu He, Xiaofang Liu, Rongfeng Li, Bai Yang, Kaili Yu, Min Zeng & Ronghai Yu

Received: 27 November 2015

Accepted: 09 February 2016

Published: 03 March 2016

$\text{Ce}^{3+}$ -doped yttrium aluminum garnet (YAG:Ce) nanocrystals were successfully synthesized via a facile sol-gel method. Multiple characterization techniques were employed to study the structure, morphology, composition and photoluminescence properties of YAG:Ce nanophosphors. The YAG:Ce<sub>0.0055</sub> sintered at 1030 °C exhibited a typical  $5d^1-4f^1$  emission band with the maximum peak located at 525 nm, and owned a short fluorescence lifetime  $\tau_1$  (~28 ns) and a long fluorescence lifetime  $\tau_2$  (~94 ns). Calcination temperature and  $\text{Ce}^{3+}$  doping concentration have significant effects on the photoluminescence properties of the YAG:Ce nanophosphors. The emission intensity was enhanced as the calcination temperature increased from 830 to 1030 °C, but decreased dramatically with the increase of  $\text{Ce}^{3+}$  doping concentration from 0.55 to 5.50 at.% due to the concentration quenching. By optimizing the synthesized condition, the strongest photoluminescence emission intensity was achieved at 1030 °C with  $\text{Ce}^{3+}$  concentration of 0.55 at.%.

The energy-efficient white light-emitting diode (WLED) has been widely applied as a solid-state optical source in various fields such as general lighting, car lighting backlighting sources, apparatus display screen and so on<sup>1–6</sup>. Generally, white light can be produced through three approaches: a blue LED combining with yellow phosphors, an ultraviolet LED matching with mixture of yellow (or red and green) phosphors and blue phosphors, and a device consisting of red, green and blue LEDs<sup>7–10</sup>. Among them, the blue LED plus yellow phosphor system is prior selected as the commercial WLEDs due to its facile fabrication and low cost, as well as nice colour-rendering index (CRI)<sup>10</sup>. Since the YAG:Ce phosphor was firstly used in displays by Blasse *et al.*<sup>11</sup> in 1967, it widely acted as a classical down-conversion material because of its high quantum efficiency, high refractive index, good mechanical strength, outstanding chemical and thermal stability.

Traditionally, YAG:Ce phosphors are easily agglomerated via solid-state reaction at high temperature (>1500 °C) and thus post-milling is required, which would cause the disadvantages of oversize grains and incorporation of impurities<sup>11–13</sup>. Although molten salt method can efficiently reduce calcination temperature, the postprocessing becomes more complex<sup>14</sup>. In order to overcome the above shortcomings, wet-chemical synthetic approaches have been developed for fabricating pure and homogeneous YAG:Ce phosphors. For instance, He *et al.*<sup>15,16</sup> obtained YAG:Ce phosphors by spray pyrolysis method and could randomly control the grain size and composition of product particles with nano/microsphere morphology. Murai *et al.*<sup>17</sup> synthesized uniform  $\text{Y}_3\text{Al}_5\text{O}_{12}:\text{Ce}$  nanocrystals with a particle size less than 50 nm by sol-gel route. Jiao *et al.*<sup>18</sup> successfully synthesized pure nano-scale Ce-doped YAG phosphors via LiF assisted sol-gel method at a lower temperature of 540 °C. Thus, sol-gel method, which is simple and controllable, is widely used in fabrication of YAG:Ce phosphors. The blue absorption and yellow emission of the  $\text{Ce}^{3+}$ -doped YAG phosphors, which are attributed to  $4f^1 \rightarrow 4f^05d^1$  and  $4f^05d^1 \rightarrow 4f^1$  transitions of  $\text{Ce}^{3+}$  ion<sup>19</sup>, respectively. The participation of  $5d$  energy levels makes the transitions be sensitive to the crystal field environment and the site symmetry of the host lattice, i.e. local structure of  $\text{Ce}_Y$  substitution. Therefore, both of the emission intensity and wavelength depend on the local structure and distribution of the  $\text{Ce}_Y$  in YAG:Ce phosphors<sup>20,21</sup>. George *et al.*<sup>22</sup> studied the local environment of  $\text{Ce}^{3+}$  activators in  $\text{Y}_3\text{Al}_5\text{O}_{12}:\text{Ce}$  phosphors and found that the random distribution of  $\text{Ce}^{3+}$  ions in YAG lattice could result in the slight expansion of YAG unit cell, which played critical roles in enhancing quantum yield and preventing from photoluminescence quenching. Belén *et al.*<sup>23</sup> studied the interplay between the  $\text{Ce}_Y$  and  $\text{Y}_{\text{Al}}-\text{Al}_Y$  in YAG by using the first-principles calculations and found that the presence of  $\text{Y}_{\text{Al}}-\text{Al}_Y$  could cause a strongly anisotropic

School of Materials Science and Engineering, Beihang University, Beijing, 100191, P. R. China. Correspondence and requests for materials should be addressed to X.-F.L. (email: liuxf05@buaa.edu.cn) or R.-H.Y. (email: rhyu@buaa.edu.cn)

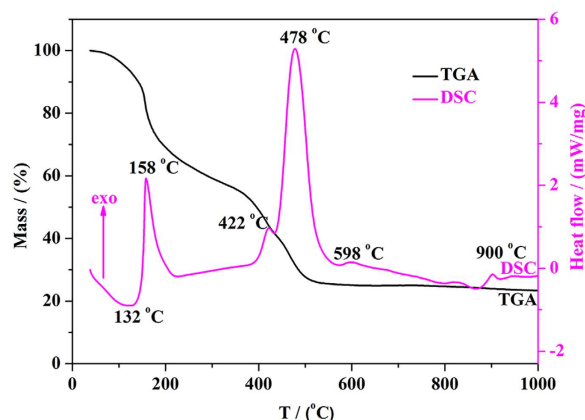


**Figure 1.** DSC-TGA profiles for the thermal variation in the precursor of sample-1.

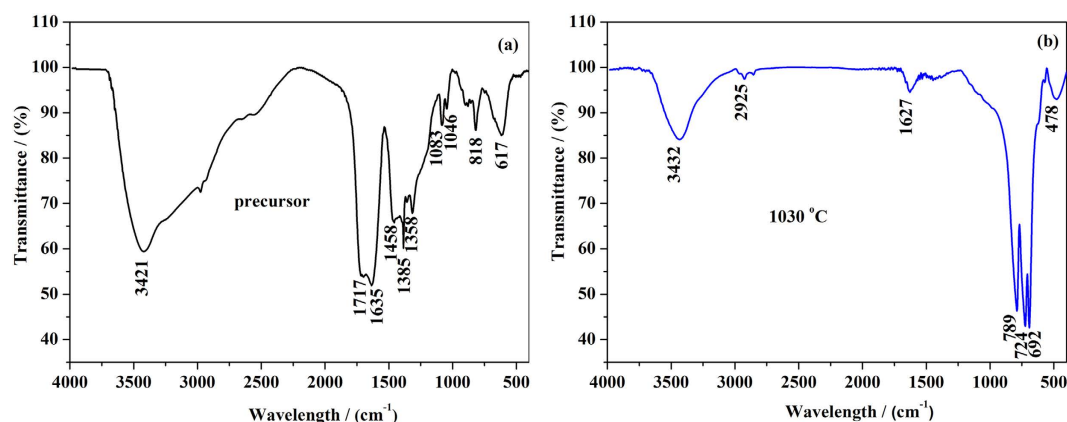


**Figure 2.** FT-IR spectra: (a) the precursor of YAG:Ce sample-1 (100 °C, 24 h) and (b) the powder of YAG:Ce sample-1 (1030 °C, 3 h).

expansion of the atomistic structure around the  $Ce_Y$  impurities and decrease the effective ligand-field splitting of the  $5d_1$  manifold, leading to the blue-shifts the two lowest  $Ce^{3+}$  4f–5d transitions. Although the photoluminescence properties of  $Ce^{3+}$  ions in garnet structure were investigated<sup>24</sup>, the detailed relationship between the photoluminescence properties and the local structures as well as the distributions of activators in  $Ce^{3+}$ -doped YAG phosphors have been rarely studied experimentally.

In this work, a series of YAG:Ce nanocrystalline phosphors were prepared by sol-gel method<sup>25</sup> in terms of its advantages of uniform distribution of  $Ce^{3+}$  ions, fast reaction rate and low calcination temperature. The composition, structure and morphology of the YAG:Ce<sub>x</sub> nanophosphors were well tuned by changing the  $Ce^{3+}$  concentration and the calcination temperature, aiming to enhance their emission intensity. Using multiple characterization techniques, we systematically clarified the intrinsic relationship among composition, structure and property.

## Results and Discussion

**Phase formation and crystal structure.** Figure 1 shows the DSC-TGA curves corresponding to the agglomeration process of YAG:Ce sample-1 from precursors to phosphors. The DSC curve exhibits the first endothermic peak at 132 °C, which originates from the evaporation of residual water. The strong exothermic peak at 158 °C is probably ascribed to the elimination of chelating agent molecules. Moreover, two intense exothermic peaks around 422 and 478 °C could be attributed to the pyrolysis of organic compounds and degradation of intermediate species formed during the gelation process, respectively<sup>26</sup>. From the TGA curve, it is found that a considerable weight loss in stages occurred with increasing temperature before 598 °C and the total weight loss was ~75 wt.%. However, the TGA curve almost keeps constant when the sintering temperature is above 598 °C. This phenomenon indicates the beginning of crystallization<sup>21</sup>, which is further confirmed by the appearance of exothermic peak at 900 °C. Thus, the crystallization temperature of YAG:Ce phosphors synthesized via sol-gel method is probably in the range of 830–900 °C.

The FT-IR spectrum of YAG:Ce sample-1 precursor is shown in Fig. 2(a). The intense and broad envelope of band at  $\sim 3421\text{ cm}^{-1}$  is due to the O–H vibration caused by  $H_2O$  in the sample<sup>27</sup>. The absorption bands at 1635 and  $1458\text{ cm}^{-1}$  should be ascribed to stretching vibrations of the –COO– groups<sup>20</sup>. Comparing with the standard citric acid (at  $1717\text{ cm}^{-1}$ ), these –COO– groups shift to lower frequency because of the coordination of –COO– groups and metal ions. The strong absorption bands at  $1385\text{ cm}^{-1}$  originate from the surface-adsorbed nitrate groups<sup>20</sup>.

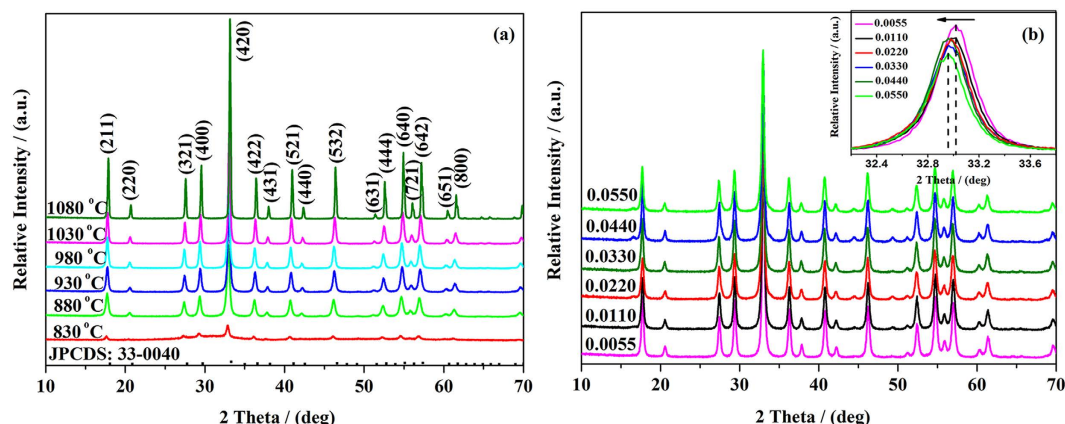


**Figure 3.** The XRD patterns of (a) YAG:Ce sample-1 sintered at different temperatures for 3 h and (b) YAG:Ce samples sintered at 1030 °C for 3 h with different Ce<sup>3+</sup> concentration.

The absorption bands at 1083 and 1046 cm<sup>-1</sup> could be attributed to O-H bend<sup>20</sup>. Moreover, the several broad bands observed within the 550–850 cm<sup>-1</sup> region of the IR spectrum correspond to M-O bonds (M = Y or Al) vibrations in the precursor<sup>28</sup>. The FT-IR spectrum of YAG:Ce sample-1 is presented in Fig. 2(b). The intense and broad envelope of bands at ~3432 cm<sup>-1</sup> is due to the stretching vibration of adsorbed H<sub>2</sub>O. The peaks at ~789 and ~692 cm<sup>-1</sup> are the characteristic vibrations of Al-O (metal-oxygen) while the peaks at ~724 and ~478 cm<sup>-1</sup> represent the Y-O (metal-oxygen) vibrations<sup>26</sup>. The presence of intensive vibration peaks of Y-O and Al-O suggests that the YAG:Ce sample-1 was crystallized at 1030 °C.

Figure 3(a) displays the XRD patterns of the YAG:Ce sample-1 sintered at different temperatures. The positions of the diffraction peaks for the six samples are similar and consistent with the standard cubic structure of Y<sub>3</sub>Al<sub>5</sub>O<sub>12</sub> (JCPDS: 33-0040) and space group Ia-3d (230)<sup>29</sup>. It implies that the pure YAG phase can be successfully obtained at a temperature as low as 830 °C and no other crystalline phases such as Y<sub>4</sub>Al<sub>12</sub>O<sub>9</sub> (YAM) or YAlO<sub>3</sub> (YAP) form. Therefore, the crystallization temperature can be effectively decreased through the sol-gel method and the lowest crystallization temperature is found to be 830 °C in our work. With the increase of calcination temperature, the diffraction peaks of YAG:Ce sample-1 become strong and sharp, demonstrating the increase of crystallinity. Meanwhile, the crystalline size can be estimated by Scherrer's formula. It was clear that the crystalline mean grain size increases with the increase of sintering temperature as shown in Table 1. Figure 3(b) shows the XRD patterns of YAG:Ce samples with different Ce<sup>3+</sup>-doped concentration sintered at 1030 °C. All the diffraction peaks can be indexed as YAG phase and no impurity peaks are detected, which reveals that the incorporated Ce<sup>3+</sup> ions do not change the crystalline structure of YAG. Nevertheless, the peak positions of diffraction peaks shift towards low angle region due to the larger ionic radius of Ce<sup>3+</sup> ion (1.07 Å) than that of Y<sup>3+</sup> ion (0.92 Å). It is well known that pure phase YAG:Ce phosphors with high crystallinity is critical to obtain large-powder WLEDs with high efficiency<sup>30,31</sup>. Hence, it is expected that the synthesized Ce<sup>3+</sup>-doped YAG phosphor possesses good photoluminescence property.

To confirm the formation of YAG:Ce phosphors in the cubic phase, Rietveld refinement was performed on the XRD patterns using the Fullprof 2K software. Figure 4 presents the Rietveld refinement results for the YAG:Ce sample-1 sintered at different temperatures and the YAG:Ce sample-1, -2 and -3 with different Ce<sup>3+</sup> doped concentration, respectively, and simultaneously the crystallographic data are summarized in Table 1. It can be seen from Fig. 4(a–d) that the unit cell parameters (*a*) decreased with increasing calcination temperature, keeping accordance with the shift of the position of diffraction peak to larger angle in the XRD patterns<sup>20</sup>. Meanwhile, the results from Fig. 4(d–f) show that the unit lattice parameters (*a*) become larger with increasing Ce<sup>3+</sup> concentration due to the larger Ce<sup>3+</sup> ionic radius than that of Y<sup>3+</sup> ion. It suggests that the unit cell parameters of YAG:Ce nanocrystalline could be expanded with increasing the amount of Ce<sup>3+</sup> ions into Y lattice sites gradually.

The high-resolution magic angle spinning (MAS) <sup>27</sup>Al NMR spectroscopy was carried out for identifying the different phases and coordination states of Al sites in Al-containing materials because of the high sensitivity of <sup>27</sup>Al NMR chemical shift towards the local chemical environment of Al nucleus, especial for the material with short range order where powder XRD provided little information about the Al distribution<sup>32,33</sup>. Figure 5(a) provides the <sup>27</sup>Al MAS NMR spectra of YAG (down) and YAG:Ce sample-1 (up) sintered at 1030 °C for 3 h. The sharp and narrow line at 0.9 ppm observed for both of YAG and YAG:Ce sample-1 could be assigned to the octahedral AlO<sub>6</sub> species<sup>32</sup>. Another weak signal at -16.9 ppm is located within chemical shift range of AlO<sub>6</sub> species as well<sup>33,34</sup>. From the relative intensity of these two peaks, it is concluded that the weak line at -16.9 ppm arises from the AlO<sub>6</sub> units suffering from the chemical influence of the tiny amount of Ce<sup>3+</sup> ions, keeping accordance with the previous literature<sup>22</sup>. Its chemical shift to higher field relative to typical AlO<sub>6</sub> species (0.9 ppm) was caused by the adjacent Ce<sup>3+</sup> whose unpaired electrons in the 4f shell influence the local magnetic field of adjacent Al nuclei, which is further supported by the absence of peak at -16.9 ppm in the spectrum of the YAG without Ce<sup>3+</sup> ions doping (Fig. 5(a) down). Additionally, the other broad peak appeared at 47.0–68.3 ppm can be attributed to the second-order quadrupole line shape of hexahedral AlO<sub>6</sub> species due to the lower symmetry of the crystallographic site with respect to the octahedral AlO<sub>6</sub> units<sup>34,35</sup>. And it was confirmed further by the high-resolution <sup>27</sup>Al MQ MAS NMR spectrum as illustrated in Fig. 5(b), where the isotropic F1 projection showed considerably

Atomic parameters of YAG:Ce <sub>x</sub> sample-1							
Atoms	Wyckoff	x/a	y/b	z/c	Cell parameter (Å)	Cell volume (Å) <sup>3</sup>	Mean size (Å)
Al 1	16a	0.00000	0.00000	0.00000	12.0354	1743.336	208
Al 2	24d	0.37500	0.00000	0.25000			
Y 1	24c	0.12500	0.00000	0.25000			
Ce 1	24c	0.12500	0.00000	0.25000			
O 1	96h	−0.02985	0.05056	0.14878			
Al 1	16a	0.00000	0.00000	0.00000	12.0220	1737.523	238
Al 2	24d	0.37500	0.00000	0.25000			
Y 1	24c	0.12500	0.00000	0.25000			
Ce 1	24c	0.12500	0.00000	0.25000			
O 1	96h	−0.03139	0.05148	0.14915			
Al 1	16a	0.00000	0.00000	0.00000	12.0198	1736.557	243
Al 2	24d	0.37500	0.00000	0.25000			
Y 1	24c	0.12500	0.00000	0.25000			
Ce 1	24c	0.12500	0.00000	0.25000			
O 1	96h	−0.02998	0.05117	0.14989			
Al 1	16a	0.00000	0.00000	0.00000	12.0079	1731.408	310
Al 2	24d	0.37500	0.00000	0.25000			
Y 1	24c	0.12500	0.00000	0.25000			
Ce 1	24c	0.12500	0.00000	0.25000			
O 1	96h	−0.03161	0.05207	0.14913			
Al 1	16a	0.00000	0.00000	0.00000	12.0093	1732.026	270
Al 2	24d	0.37500	0.00000	0.25000			
Y 1	24c	0.12500	0.00000	0.25000			
Ce 1	24c	0.12500	0.00000	0.25000			
O 1	96h	−0.03177	0.05011	0.14924			
Al 1	16a	0.00000	0.00000	0.00000	12.0197	1736.522	268
Al 2	24d	0.37500	0.00000	0.25000			
Y 1	24c	0.12500	0.00000	0.25000			
Ce 1	24c	0.12500	0.00000	0.25000			
O 1	96h	−0.03259	0.04875	0.14842			

**Table 1.** Crystallographic data with atomic parameters of YAG:Ce<sub>x</sub> samples.

improved resolution and it was clear that only two different coordinated Al species, i.e. AlO<sub>4</sub> groups and AlO<sub>6</sub> units, could be observed. Thus, the possible presence of alumina or any other aluminate such as five-fold coordinated Al sites<sup>35–37</sup> can be excluded, keeping consistent with the previous XRD analysis. As a result, the structure of the YAG:Ce sample-1 can be depicted as following: YAG:Ce consists of a network of octahedral AlO<sub>6</sub> and hexahedral AlO<sub>4</sub> groups in which the yttrium atoms are located in the dodecahedral interstices formed by the corner sharing arrangement of the AlO<sub>4</sub> and AlO<sub>6</sub> polyhedra, and the incorporated Ce<sup>3+</sup> ions substitute for a part of Y<sup>3+</sup> ions.

**Morphology and microstructure.** The SEM images of the YAG:Ce samples prepared at different temperatures are shown in Fig. 6. It is clear that these samples possess high dispersity. The mean size (*D*) values of the YAG:Ce samples measured from the SEM images are listed in Table 2. The *D* values of the YAG:Ce samples increase from ~60 to ~120 nm as the calcination temperature rises, which agrees with the XRD results<sup>13,38</sup>. In addition, Fig. 6(e,g–i) provides the SEM images of YAG:Ce samples sintered at 1030 °C with Ce<sup>3+</sup>-doped concentrations of 0.55, 1.10, 3.30 and 5.50 at.%. The mean size of the nanoparticles is ~95 nm and it is almost independent on the Ce<sup>3+</sup> doping concentration.

The detailed morphology, microstructure and composition of the YAG:Ce sample-1 sintered at 1030 °C for 3 h were further analyzed by TEM, HRTEM and EDX. From Fig. 7(a), it is observed that the nanoparticles are homogeneous and well dispersed with uniform morphology. The average size of the particles is 93 nm, keeping accordance with the results from SEM characterization. Figure 7(b) shows the HRTEM image of YAG:Ce sample-1. The interplanar spacing of the lattice fringes *d*<sub>211</sub> is estimated to be 0.4924 nm which is larger than the standard value of YAG (*d*<sub>211</sub> = 0.4905 nm, JCPDS: 33–0040)<sup>39–41</sup>. The EDS spectrum in Fig. 7(c) confirms the presence of yttrium (Y), aluminum (Al), oxygen (O) and cerium (Ce) elements in the YAG:Ce sample-1. Except for the Cu peak resulting from the copper mesh, no other impurity can be detected in the sample.

**Chemical state at the surface.** The XPS surface measurement was applied to analyze the composition and the valence state of the incorporated Ce ions at the surface region of YAG:Ce sample-1 as shown in Fig. 8. The

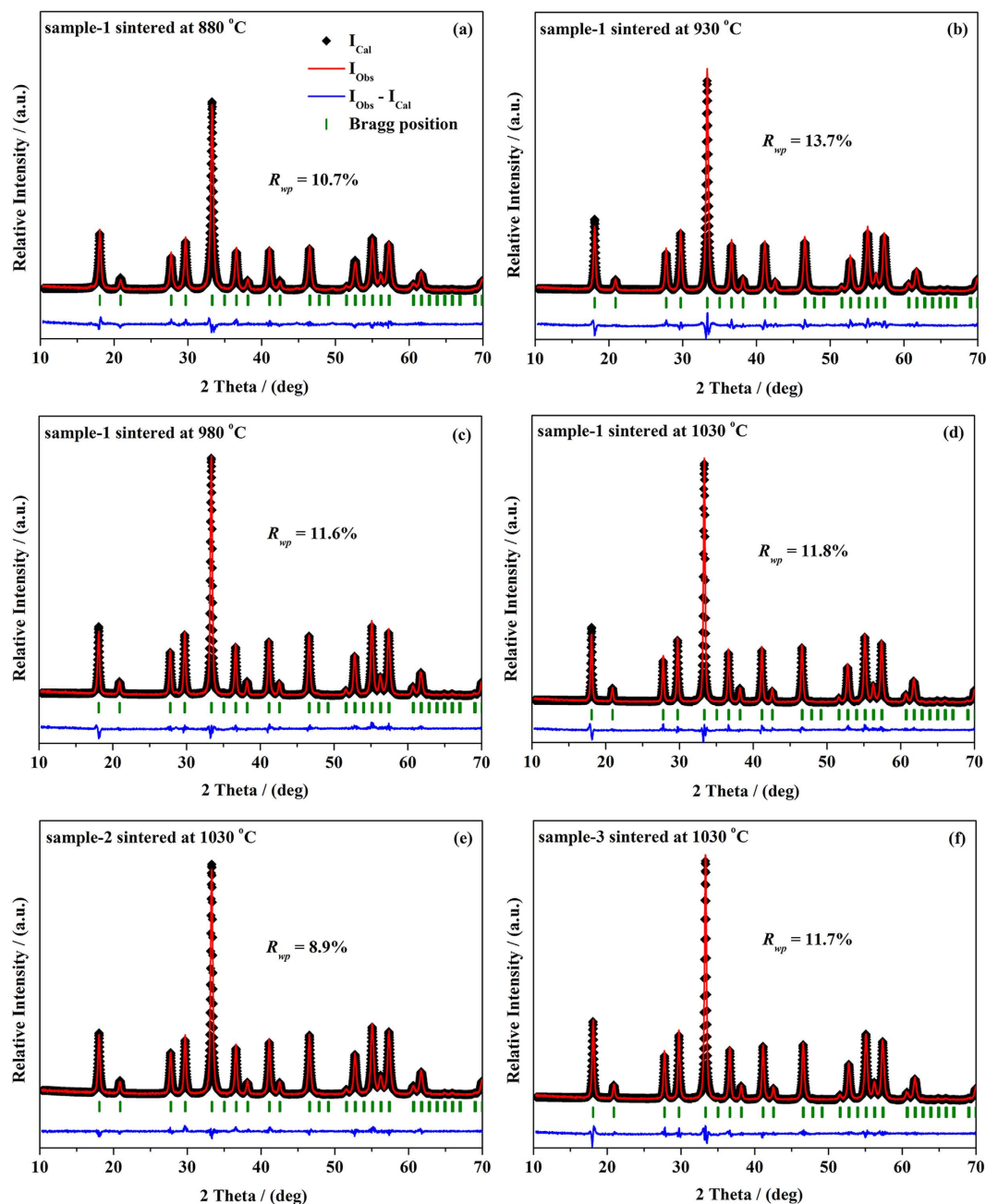


**Figure 4. Rietveld refinement.** (a–d) YAG:Ce sample-1 sintered at different temperatures for 3 h and (d–f) YAG:Ce sample-1, -2 and -3 sintered at 1030 °C for 3 h with different Ce<sup>3+</sup> concentration.

Ce3d XPS spectrum exhibits two sets of doublets ( $3d_{5/2}$  at 881.9 eV and 885.3 eV;  $3d_{3/2}$  at 899.2 eV and 903.3 eV) which are primarily attributed to +3 oxidation state of cerium<sup>26,42–44</sup>. However, the appearance of another weak highest binding energy peak locating at 916.7 eV reveals the existence of a few Ce<sup>4+</sup> species<sup>44</sup>. It is reasonable that a few cerium-(III) species were oxidized to cerium-(IV) species on the surface of the sample as it was sintered in the air.

**Photoluminescence properties and energy transfer.** The PLE spectra ( $\lambda_{em} = 525$  nm) of the YAG:Ce sample-1 sintered under different temperatures were measured in the wavelength range of 300–500 nm and shown in Fig. 9(a). Two prime excitation peaks are located at ~344 and ~454 nm, deriving from the  $4f^1 ({}^2F_{7/2}) \rightarrow 4f^0 5d^1$  electron transitions of Ce<sup>3+</sup> ions. The shape and position of excitation peaks are nearly independent on calcination temperature. However, the PLE intensity increases with the increase of calcination temperature and exhibits the maximum excitation at 1030 °C. The excitation peak at 454 nm matches well with the blue emitting from InGaN-based LEDs. Thus, it reveals that the YAG:Ce sample-1 can efficiently absorb the blue emission and match well with InGaN LEDs.



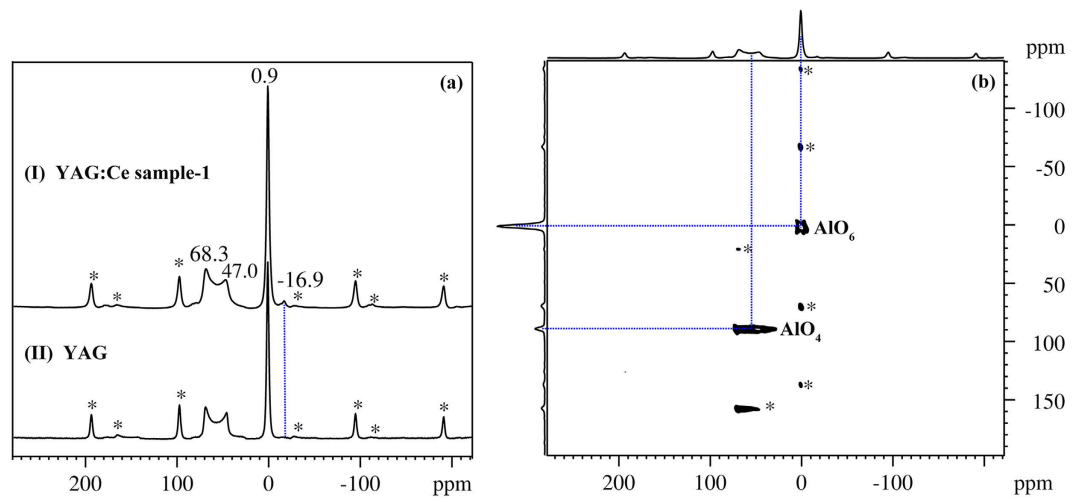


**Figure 5.** (a)  $^{27}\text{Al}$  MAS NMR spectra of YAG and YAG:Ce sample-1 and (b)  $^{27}\text{Al}$  3Q MAS NMR spectrum of YAG:Ce sample-1 sintered at  $1030^\circ\text{C}$  for 3 h. Spin rate was 10 kHz and the asterisks stand for spinning bands.

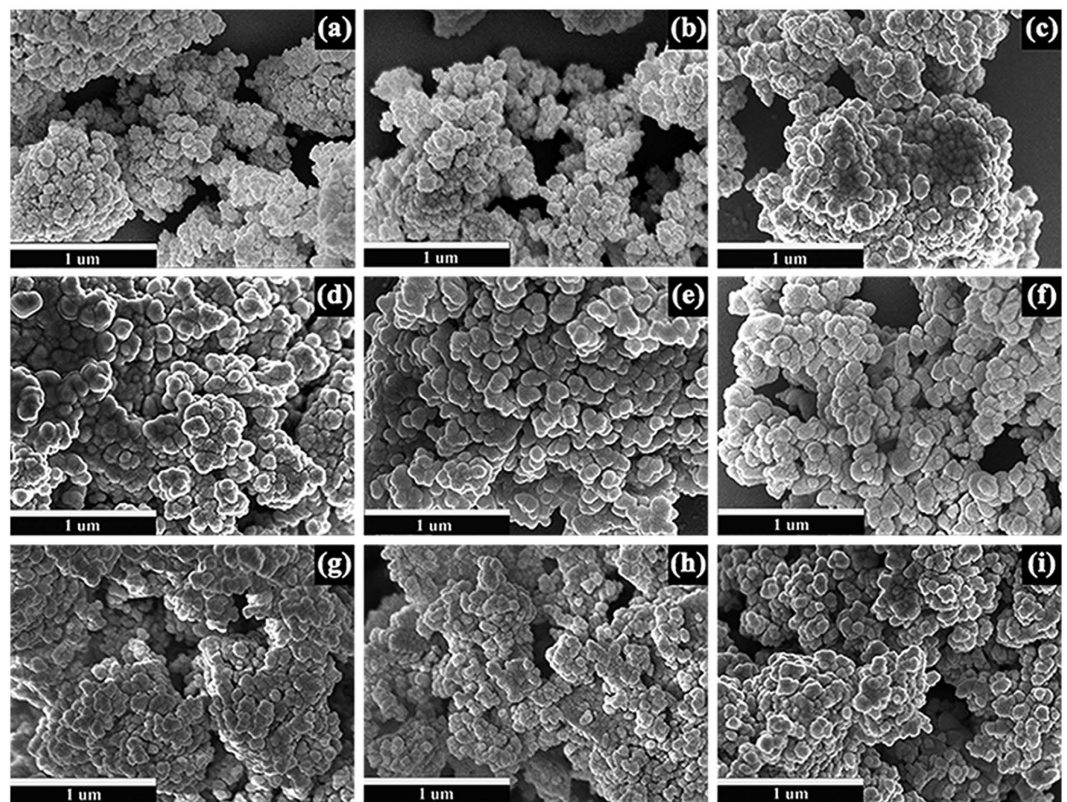


**Figure 6.** SEM images: (a–f) YAG:Ce sample-1 sintered at different temperatures for 3 h and (e,g–i) YAG:Ce samples with different  $\text{Ce}^{3+}$ -doped concentrations sintered at  $1030^\circ\text{C}$  for 3 h.

Samples	a	b	c	d	e	f	g	h	i
T ( $^\circ\text{C}$ )	830	880	930	980	1030	1080	1030	1030	1030
$\text{Ce}^{3+}$ (at.%)	0.55	0.55	0.55	0.55	0.55	0.55	1.10	3.30	5.50
D (nm)	61	66	75	84	95	118	91	90	93

**Table 2.** The mean size (D) values of YAG:Ce samples.

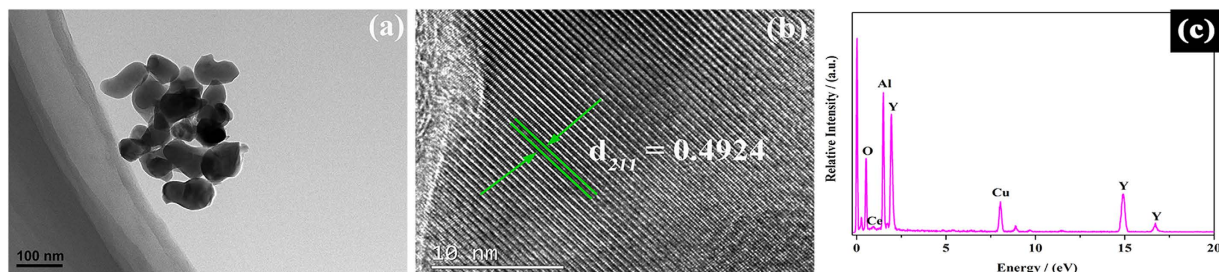


**Figure 7.** The TEM image, (b) HRTEM image and (c) EDX result of YAG:Ce sample-1 (1030 °C, 3 h).

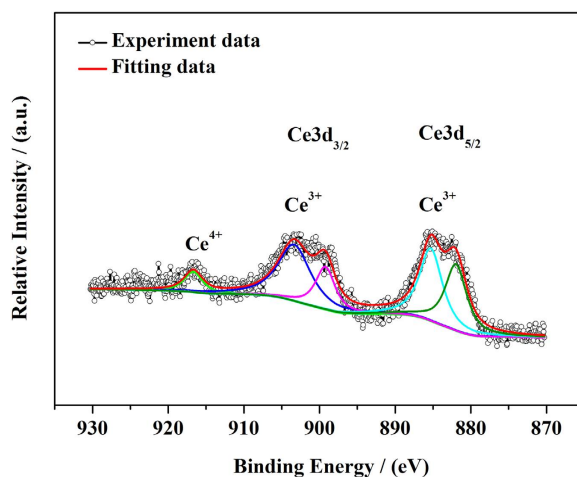


**Figure 8.** The XPS spectrum of Ce3d electrons in YAG:Ce sample-1 (1030 °C for 3 h).

Figure 9(b) shows the PL emission spectra ( $\lambda_{\text{ex}} = 454 \text{ nm}$ ) of the YAG:Ce sample-1 sintered at different temperatures. A typical broad emission band centered at  $\sim 525 \text{ nm}$  is seen in all the samples. It is clear that the PL emission intensity strongly depends on the calcination temperature. As the calcination temperature rises from 830 to 1030 °C, the position of the PL peak shows negligible change, however, the PL emission intensity significantly increases and reaches the maximum value at 1030 °C (shown in the inset of Fig. 9(b)). The increase of emission intensity with calcination temperature is due to the improvement of crystallinity by thermal treatment, and thus more  $\text{Ce}^{3+}$  ions entering  $\text{Y}^{3+}$  lattice can be efficiently excited in YAG:Ce sample-1. Nevertheless, the emission intensity of the sample considerably decreases when the calcination temperature further increases to 1080 °C. We presume that such decrease of emission intensity is induced by cross relaxation between the adjacent  $\text{Ce}^{3+}$  ions caused by the further decreased unit cell parameters (*a*). Meanwhile, the enlarged average nanoparticles size and increased defects could cause a higher probability of nonradiative transitions as well<sup>22,45–47</sup>.

The strongest PL emitting curve could be fitted into two components by gaussian deconvolution, centering at  $\sim 517 \text{ nm}$  (peak 1) and  $\sim 558 \text{ nm}$  (peak 2) as shown in Fig. 9(c). These two peaks correspond to the typical  $5d^1-4f^1$  ( $^2F_{5/2}$ ) and  $5d^1-4f^1$  ( $^2F_{7/2}$ ) transitions of  $\text{Ce}^{3+}$  ion, the energy difference between the two energy levels is  $\sim 1500 \text{ cm}^{-1}$  because of the spin-orbital coupling in crystal-field<sup>11,12,48</sup>.

The PL emission spectra of the YAG:Ce samples with different  $\text{Ce}^{3+}$ -doped concentrations sintered at 1030 °C for 3 h are shown in Fig. 9(d). The position of the PL peak is almost independent on the  $\text{Ce}^{3+}$  concentration, but the PL emission intensity decreases dramatically (inset of Fig. 9(d)) as the  $\text{Ce}^{3+}$  concentration increases from 0.55 to 5.50 at.%. The YAG:Ce phosphors exhibit the strongest PL emission when the  $\text{Ce}^{3+}$  ion concentration is 0.55 at.%, agreeing with the previous investigations<sup>31,49</sup>. Additionally, Zhang *et al.*<sup>21,50</sup> studied PL intensity of YAG:Ce with lower  $\text{Ce}^{3+}$  at.% doping and found that the suitable  $\text{Ce}^{3+}$  at.% doping concentration is from 0.05 to 1 at.%. As evidenced by the previous Rietveld analysis of XRD patterns and NMR spectrum, the co-doped  $\text{Ce}^{3+}$  ion substitutes for  $\text{Y}^{3+}$  ion which is located in the dodecahedral position of YAG, and the symmetrical characteristic is  $D_2$ <sup>48,51,52</sup>. Accompanying with the increasing  $\text{Ce}^{3+}$  doping concentration, the unit cell parameters (*a*) increased certainly, which may enlarge the distance among  $\text{Ce}^{3+}$  ions in the structure of the YAG:Ce nanocrystal. In this case, however, more nonradiation can be induced by cross relaxation of the excessive  $\text{Ce}^{3+}$  dopant. Generally, the effect of crystal field on the *4f* state of  $\text{Ce}^{3+}$  ion is rather weak due to the shielding effect of the outer *5p* and *6s* electrons. Therefore, it maintains the two separate features of free ion energy levels. Whereas the *5d* state is intensively influenced by the local crystal field surrounding the  $\text{Ce}^{3+}$  ion. Hence the *d*  $\rightarrow$  *f* emission band is dependent on the local crystal field surrounding the  $\text{Ce}^{3+}$  ion<sup>48</sup>. Firstly, the high doping concentration hinders the substitution of  $\text{Ce}^{3+}$  ions for  $\text{Y}^{3+}$  ions owing to the large difference of ionic radius. Thus, the excessive  $\text{Ce}^{3+}$  incorporation results in more short average distance among  $\text{Ce}^{3+}$  ions and increases the probability of non-radiative transitions,

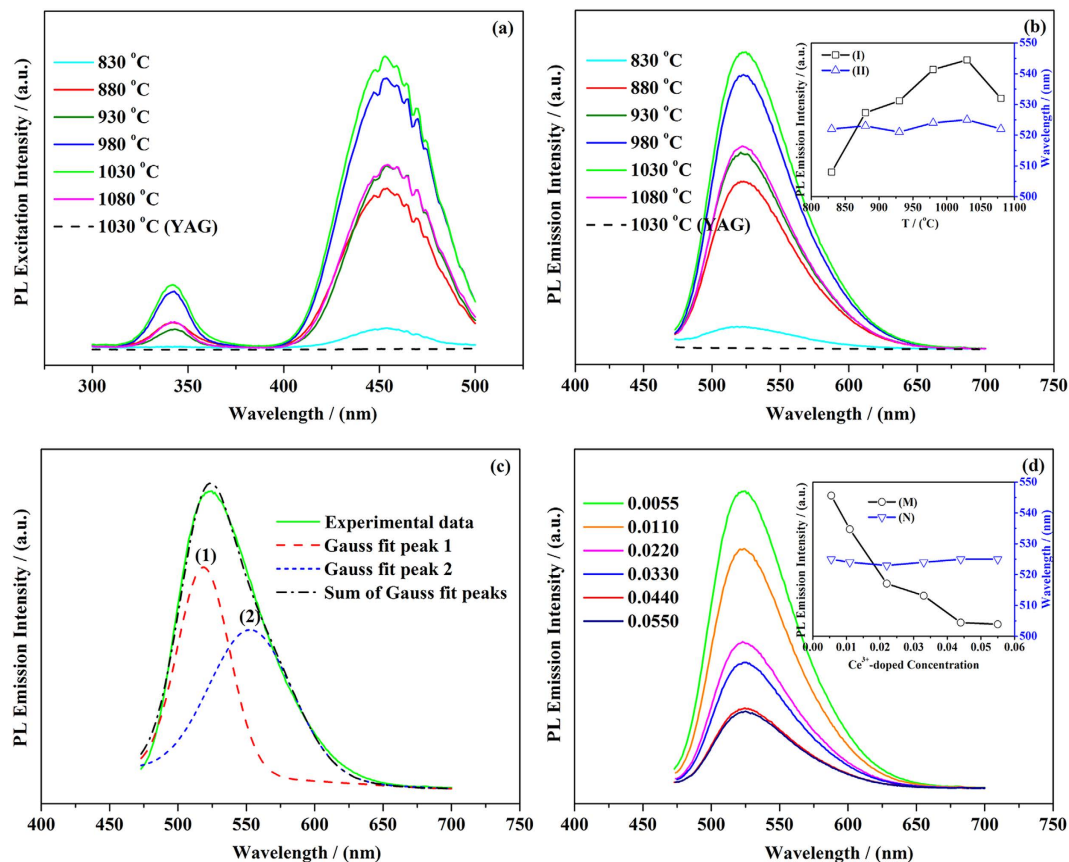


**Figure 9.** (a) The PLE and (b) PL spectra spectra of pure YAG (dash line) and YAG:Ce sample-1 sintered at different temperatures for 3 h ( $\lambda_{em} = 525$  nm). The inset in Fig. 8(b): variation of PL intensity (I) and emission peak position (II) with the calcination temperature. (c) The gaussian fitted (dashed) and decomposed components (dotted) of the PL spectra of YAG:Ce sample-1 (1030 °C, 3 h). (d) The PL emission spectra of YAG:Ce samples with different  $Ce^{3+}$ -doped concentrations (1030 °C, 3 h). Inset of Fig. 8(d): variation of PL intensity (M) and emission peak position (N) with different  $Ce^{3+}$ -doped concentrations ( $\lambda_{ex} = 454$  nm).

Sample	Temperature	Lifetime $\tau_1$ (ns)	Lifetime $\tau_2$ (ns)
YAG:Ce sample-1	1030	27.8	94.0
YAG:Ce sample-1	1080	26.5	91.1
YAG:Ce sample-6	1030	18.0	52.3

**Table 3.** Decay times of YAG:Ce phosphors.

thus inducing concentration quenching of  $Ce^{3+}$  ions. Secondly, the oxidation of the cerium ions ( $Ce^{3+} \rightarrow Ce^{4+}$ ) occurred near the surface can reduce the photoluminescence intensity of the  $Ce^{3+}$  activators<sup>19,53</sup>. Thirdly, for YAG phosphors with high  $Ce^{3+}$  concentration, another reason for the reduction of PL intensities is the partial absorption of excitation photons by YAG host. The competition makes less  $Ce^{3+}$  ions be excited and thus weakens the PL intensity of the YAG:Ce phosphors. To avoid the above problems, a suitable  $Ce^{3+}$  concentration and a homogeneous distribution of activators in the YAG host are important for obtaining high efficiency and brightness in the YAG:Ce system with small amount of  $Ce^{3+}$ .

**The decay of photoluminescence lifetime.** Fig. S1 shows the PL decay curves of YAG:Ce samples with different  $Ce^{3+}$  doping concentrations sintered at 1030 and 1080 °C. These curves can be fitted using a double-exponential function  $I = A_1 \exp(-t/\tau_1) + A_2 \exp(-t/\tau_2) + I_0$ <sup>19,54,55</sup>, where  $A_1$  and  $A_2$  are the corresponding initial intensities of the pulse shape components and  $I_0$  is a time independent background intensity<sup>55</sup>. The decay includes two exponential terms, a short lifetime  $\tau_1$  and a long lifetime  $\tau_2$ , as listed in Table 3. Among them,  $\tau_1$  is likely due to the quenching of  $Ce^{3+}$  by the defects at the surface of nanoparticles, while  $\tau_2$  is assigned to  $Ce^{3+}$  inside the crystalline nanoparticles<sup>19,56</sup>. The large specific surface area of the nanoparticles has profound effects on the photoluminescence properties because of the partial oxidation of activator  $Ce^{3+}$  to  $Ce^{4+}$  on the surface. Since



more surface defects formed due to the increase of specific surface area, the PL lifetime of  $\text{Ce}^{3+}$ -doped YAG was shortened than that of the ideal YAG:Ce crystal<sup>55,56</sup>.

As shown in Table 3, both  $\tau_1$  and  $\tau_2$  of the YAG:Ce sample-1 are slightly shortened when the calcination temperature increased from 1030 to 1080 °C. The slight variation of PL lifetime could be attributed to the further oxidation of cerium ion ( $\text{Ce}^{3+} \rightarrow \text{Ce}^{4+}$ ) by the excessive calcination, which is consistent with the result of PL characterization (shown in Fig. 9(b)). Therefore, an appropriate calcination temperature is favorable to achieving strong PL emission and decreasing the PL decay. Moreover, it can be found in Table 3 that the PL lifetimes (both  $\tau_1$  and  $\tau_2$ ) of YAG:Ce sample-6 are much shorter than that of the YAG:Ce sample-1. Generally, the PL lifetime  $\tau$  can be written as  $\tau = (\gamma_r + \gamma_{nr})^{-1}$ , where  $\gamma_r$  is the decay rate of radiative process and  $\gamma_{nr}$  is the rate of non-radiative process<sup>54,56</sup>. In the  $\text{Ce}^{3+}$ -doped YAG phosphors, the substitution of  $\text{Ce}^{3+}$  ions for  $\text{Y}^{3+}$  ions results in the creation of structural defects such as surface  $\text{Ce}^{4+}$ , non-luminescent aggregates of  $\text{Ce}^{3+}$  ions,  $\text{Y}_{\text{Al}}$  antisite defects and so on<sup>57</sup>, which could act as the quenching center of luminescence<sup>56</sup>. Consequently, the increase of  $\text{Ce}^{3+}$  concentration would enhance the non-radiative transition. According to the above equation, larger  $\gamma_{nr}$  of the YAG:Ce sample-6 gives rise to a shorter lifetime  $\tau$  relative to YAG:Ce sample-1. Therefore, it is seen from Fig. 9(d) that the superfluous  $\text{Ce}^{3+}$  incorporation leads to PL quenching and decreases the PL intensity, i.e. increases the PL decay considerably. From the above investigation, we clarified the relationship between local structure of  $\text{Ce}^{3+}$  ions in YAG:Ce phosphors and photoluminescence properties. Meanwhile, we obtained a good YAG:Ce photoluminescence material by precisely adjusting the  $\text{Ce}^{3+}$  concentration and the calcination temperature.

## Conclusion

Nanocrystalline YAG:Ce phosphors with good dispersity were successfully prepared by sol-gel method. The photoluminescence properties of the YAG:Ce nanophosphors was adjusted by changing the calcination temperature and the  $\text{Ce}^{3+}$  concentration. It was found that the photoluminescence emission intensity of YAG:Ce nanophosphor was enhanced with the increase of calcination temperature in the range of 830–1030 °C, while dramatically decreased with the increase of  $\text{Ce}^{3+}$ -doped concentration. The strongest photoluminescence emission band centering at 525 nm was obtained in YAG:Ce<sub>0.0055</sub> nanophosphors sintered at 1030 °C for 3 h. Moreover, the studies on fluorescence lifetime suggested that the decay contained two exponential terms, i.e. the short lifetime  $\tau_1$  (~28 ns) and the long lifetime  $\tau_2$  (~94 ns). The fluorescence lifetime was not sensitive to the calcination temperature, but decreased markedly with the increase of  $\text{Ce}^{3+}$ -doped concentration. This study not only provides a good YAG:Ce photoluminescence material but also benefits the clarification of the relationship between local structure of incorporated  $\text{Ce}^{3+}$  and photoluminescence properties.

## Experimental Procedure

**Preparation of  $(\text{Y}_{1-x}\text{Ce}_x)_3\text{Al}_5\text{O}_{12}$  (YAG:Ce<sub>x</sub>) phosphors.** All reagents are of analytical grade and used without further purification. The precursors were synthesized by sol-gel method using  $\text{Y}(\text{NO}_3)_3 \cdot 6\text{H}_2\text{O}$ ,  $\text{Ce}(\text{NO}_3)_3 \cdot 6\text{H}_2\text{O}$  and  $\text{Al}(\text{NO}_3)_3 \cdot 9\text{H}_2\text{O}$  as cation resource, citric acid (CA) and ethylene glycol (EG) as chelating agents with a ratio of Cations: CA: EG = 2: 2: 1. The  $\text{Y}(\text{NO}_3)_3 \cdot 6\text{H}_2\text{O}$  and  $\text{Al}(\text{NO}_3)_3 \cdot 9\text{H}_2\text{O}$  were firstly dissolved in 120 mL distilled water with stoichiometric ratio of  $3 \times (1-x): 5$  with  $x$  varying from 0.0055 to 0.0550, and then CA and EG were added into the above solution. The solution was continuously stirred at 50 °C to evaporate excess water and accelerate the polyesterification reaction. The gels were heated in oil-bath at 100 °C for 24 h. Finally, the precursors were ground and sintered at 830, 880, 930, 980, 1030 and 1080 °C respectively for 3 h in air. The obtained YAG:Ce<sub>x</sub> phosphors were denoted as sample-1, sample-2, sample-3, sample-4, sample-5 and sample-6 corresponding to  $x$  values of 0.0055, 0.0110, 0.0220, 0.0330, 0.0440, 0.0550).

**Material characterization.** The thermal process was recorded by thermogravimetry analysis (TGA) and differential scanning calorimetry (DSC) at the heating rate of 10 °C·min<sup>-1</sup> on a Netzsch STA 449F<sup>3</sup> instrument. The FT-IR spectra of powders were measured on a Thorlabs Nicolet Nexus 6700 infrared spectrophotometer. The crystal structure of powders were characterized by X-ray diffraction (XRD) on a Rigaku D/max-2500 diffractometer using  $\text{Cu-K}_\alpha$  radiation filtered by graphite with the experimental parameters of 40 kV, 200 mA, and 6° min<sup>-1</sup>. Then Rietveld were performed on the collected data by using Fullprof 2K software to get the lattice parameters. The <sup>27</sup>Al solid state NMR spectra of the products were acquired at 104.2 MHz on a Bruker Avance III HD 400M NMR spectrometer (9.4 T) equipped a 4 mm MAS NMR probe with a spinning rate of 10 kHz. The morphology was observed by a JEOL JSM-7500F scanning electron microscope (SEM). The microstructure and composition were measured by a JEOL JEM-2100F transmission electron microscope (TEM) equipped with an Oxford energy dispersive spectrometer (EDS). The chemical state were analyzed via Thermo Scientific X-ray photoelectron spectroscopy (XPS) using a monochromatized Al-K<sub>α</sub> X-ray as the excitation source and choosing O 1s at a binding energy of 530.5 eV as the reference line. The photoluminescence emission (PL) and photoluminescence excitation (PLE) spectra of sample powders were obtained on a Hitachi F-4600 fluorescence spectrophotometer using a 150 W Xenon short-arc lamp as excitation source (wavelength range: 200–900 nm, excitation slit: 2.5 nm, emission slit: 2.5 nm, PMT voltage: 700 V). The fluorescence lifetimes (FLS) were measured by an Edinburgh FLS920 phosphorimeter using a 450 W xenon lamp. All the measurements were implemented at room temperature.

## References

- Shuji, N., Masayuki, S. & Takashi, M. P-GaN/N-InGaN/N-GaN double-heterostructure blue-light-emitting diodes. *Jpn. J. Appl. Phys.* **32**(1A), L8 (1993).
- Zhang, R. *et al.* A new-generation color converter for high-power white LED: transparent  $\text{Ce}^{3+}$ :YAG phosphor-in-glass. *Laser Photon. Rev.* **8**(1), 158–164 (2014).
- Pimpitkar, S., Speck, J. S., DenBaars, S. P. & Nakamura, S. Prospects for LED lighting. *Nat. Photon.* **3**(4), 180–182 (2009).
- Nakamura, S. The roles of structural imperfections in InGaN-based blue light-emitting diodes and laser diodes. *Science* **281**(5379), 956–961 (1998).

5. Jüstel, T., Nikol, H. & Ronda, C. New developments in the field of luminescent materials for lighting and displays. *Angew. Chem. Int. Ed.* **37**(22), 3084–3103 (1998).
6. Kobayashi, Y., Kumakura, K., Akasaka, T. & Makimoto, T. Layered boron nitride as a release layer for mechanical transfer of GaN-based devices. *Nature* **484**(7393), 223–227 (2012).
7. Jiang, Z. *et al.* Luminescence and energy transfer of single-phase and color-tunable  $\text{Ca}_2\text{Y}_3\text{Sb}_3\text{O}_{14}$ :  $\text{Bi}^{3+}$ ,  $\text{Eu}^{3+}$  phosphor for white light-emitting diodes. *J. Alloys Compd.* **650**, 598–603 (2015).
8. Schubert, E. F. & Kim, J. K. Solid-state light sources getting smart. *Science* **308**(5726), 1274–1278 (2005).
9. Lin, C. C. & Liu, R.-S. Advances in phosphors for light-emitting diodes. *J. Phys. Chem. Lett.* **2**(11), 1268–1277 (2011).
10. Yan, X. S., Li, W. W., Wang, X. B. & Sun, K. Facile synthesis of  $\text{Ce}^{3+}$ ,  $\text{Eu}^{3+}$  co-doped YAG nanoporphor for white light-emitting diodes. *J. Electrochem. Soc.* **159**(2), H195–H200 (2012).
11. Blasse, G. & Bril, A. A new phosphor for flying-spot cathod-raytubes for color television: yellow-emitting  $\text{Y}_3\text{Al}_5\text{O}_{12}\text{-Ce}^{3+}$ . *Appl. Phys. Lett.* **11**(2), 53–55 (1967).
12. Blasse, G. & Bril, A. Investigation of some  $\text{Ce}^{3+}$ -activated phosphors. *J. Chem. Phys.* **47**(12), 5139–5145 (1967).
13. Fadlalla, H. M. H., Tang, C. C., Wei, S. Y. & Ding, X. X. Preparation and properties of nanocrystalline powders in  $(\text{Y}_{1-x}\text{Ce}_x)_3\text{Al}_5\text{O}_{12}$  system. *J. Lumin.* **128**(10), 1655–1659 (2008).
14. Yang, H. J. *et al.* Characterization and luminescence properties of YAG:  $\text{Ce}^{3+}$  phosphors by molten salt synthesis. *J. Am. Ceram. Soc.* **95**(1), 49–51 (2012).
15. He, G., Mei, L., Wang, L., Liu, G. & Li, J. Synthesis and luminescence properties of nano-/microstructured  $\text{Y}_3\text{Al}_5\text{O}_{12}\text{:Ce}^{3+}$  microspheres by controlled glass crystallization. *Cryst. Growth. Des.* **11**(12), 5355–5361 (2011).
16. Purwanto, A. *et al.* High luminance YAG: Ce nanoparticles fabricated from urea added aqueous precursor by flame process. *J. Alloys Compd.* **463**(1), 350–357 (2008).
17. Murai, S., Fujita, K., Iwata, K. & Tanaka, K. Scattering-based hole burning in  $\text{Y}_3\text{Al}_5\text{O}_{12}\text{:Ce}^{3+}$  monoliths with hierarchical porous structures prepared via the sol-gel route. *J. Phys. Chem. C* **115**(36), 17676–17681 (2011).
18. Jiao, H., Ma, Q., He, L., Liu, Z. & Wu, Q. Low temperature synthesis of YAG:Ce phosphors by LiF assisted sol-gel combustion method. *Powder Technol.* **198**(2), 229–232 (2010).
19. Xu, M. M., Zhang, Z. J., Zhu, J. J., Zhao, J. T. & Chen, X. Y. Solvothermal synthesis and luminescence properties of yttrium aluminum garnet monodispersed crystallites with well-developed faces. *J. Phys. Chem. C* **118**(46), 27000–27009 (2014).
20. Xia, G., Zhou, S., Zhang, J. & Xu, J. Structural and optical properties of YAG:  $\text{Ce}^{3+}$  phosphors by sol-gel combustion method. *J. Cryst. Growth.* **279**(3–4), 357–362 (2005).
21. Zhang, L. *et al.* Citrate sol-gel combustion preparation and photoluminescence properties of YAG:Ce phosphors. *J. Rar. Earth.* **30**(4), 289–296 (2012).
22. George, N. C. *et al.* Local environments of dilute activator ions in the solid-state lighting phosphor  $\text{Y}_{3-x}\text{Ce}_x\text{Al}_5\text{O}_{12}$ . *Chem. Mater.* **25**(20), 3979–3995 (2013).
23. Munoz-Garcia, A. B., Barandiaran, Z. & Seijo, L. Antisite defects in Ce-doped YAG ( $\text{Y}_3\text{Al}_5\text{O}_{12}$ ): first-principles study on structures and 4f–5d transitions. *J. Mater. Chem.* **22**(37), 19888–19897 (2012).
24. Chen, L. *et al.* Charge deformation and orbital hybridization: intrinsic mechanisms on tunable chromaticity of  $\text{Y}_3\text{Al}_5\text{O}_{12}\text{:Ce}^{3+}$  luminescence by doping  $\text{Gd}^{3+}$  for warm white LEDs. *Sci. Rep.* **5**, 11514 (2015).
25. Pavitra, E. *et al.* Novel rare-earth-free yellow  $\text{Ca}_5\text{Zn}_{3.92}\text{In}_{0.08}(\text{V}_{0.99}\text{Ta}_{0.01}\text{O}_4)_6$  phosphors for dazzling white light-emitting diodes. *Sci. Rep.* **5**, 10296 (2015).
26. Veith, M. *et al.* Low temperature synthesis of nanocrystalline  $\text{Y}_3\text{Al}_5\text{O}_{12}$  (YAG) and Ce-doped  $\text{Y}_3\text{Al}_5\text{O}_{12}$  via different sol-gel methods. *J. Mater. Chem.* **9**(12), 3069–3079 (1999).
27. Tanner, P. A., Law, P. T. & Fu, L. S. Preformed sol-gel synthesis and characterization of lanthanide ion-doped yttria-alumina materials. *Phys. Stat. Solid. A* **199**(3), 403–415 (2003).
28. Boyer, D., Bertrand-Chadeyron, G. & Mahiou, R. Structural and optical characterizations of YAG:  $\text{Eu}^{3+}$  elaborated by the sol-gel process. *Opt. Mater.* **26**(2), 101–105 (2004).
29. Fadlalla, H. M. H. *et al.* Synthesis and characterization of photoluminescent cerium-doped yttrium aluminum garnet. *Mater. Res. Bull.* **43**(12), 3457–3462 (2008).
30. Yang, H., Lee, D.-K. & Kim, Y.-S. Spectral variations of nano-sized  $\text{Y}_3\text{Al}_5\text{O}_{12}\text{:Ce}$  phosphors via codoping/substitution and their white LED characteristics. *Mater. Chem. Phys.* **114**(2–3), 665–669 (2009).
31. Hassanzadeh-Tabrizi, S. A. Synthesis and luminescence properties of YAG:Ce nanopowder prepared by the Pechini method. *Adv. Powder Technol.* **23**(3), 324–327 (2012).
32. Alahraché, S. *et al.* Crystallization of  $\text{Y}_2\text{O}_3\text{-Al}_2\text{O}_3$  rich glasses: synthesis of YAG glass-ceramics. *J. Phys. Chem. C* **115**(42), 20499–20506 (2011).
33. Gore, K. U. *et al.*  $^{29}\text{Si}$  and  $^{27}\text{Al}$  MAS/3Q-MAS NMR studies of high silica USY zeolites. *J. Phys. Chem. B* **106**(23), 6115–6120 (2002).
34. Jung, W.-S., Ahn, S.-K. & Kim, D.-C.  $^{27}\text{Al}$  Magic-angle spinning nuclear magnetic resonance spectroscopic study of the conversion of basic dicarboxylate aluminium(III) complexes to alumina and aluminium nitride. *J. Mater. Chem.* **8**(8), 1869–1873 (1998).
35. Potdevin, A., Chadeyron, G., Boyer, D. & Mahiou, R. Sol-gel elaboration and characterization of YAG:  $\text{Tb}^{3+}$  powdered phosphors. *J. Mater. Sci.* **41**(8), 2201–2209 (2006).
36. MacKenzie, K. J. D. & Kemmitt, T. Evolution of crystalline aluminates from hybrid gel-derived precursors studied by XRD and multinuclear solid-state MAS NMR: II. Yttrium–aluminium garnet,  $\text{Y}_3\text{Al}_5\text{O}_{12}$ . *Thermochim. Acta* **325**(1), 13–18 (1999).
37. Nassar, E. *et al.* Nonhydrolytic sol-gel synthesis and characterization of YAG. *J. Mater. Chem.* **42**(7), 2244–2249 (2007).
38. Yang, H. & Kim, Y. S. Energy transfer-based spectral properties of Tb-, Pr-, or Sm-codoped YAG:Ce nanocrystalline phosphors. *J. Lumin.* **128**(10), 1570–1576 (2008).
39. Zhou, X., Zhou, K., Li, Y., Wang, Z. & Feng, Q. Luminescent properties and energy transfer of  $\text{Y}_3\text{Al}_5\text{O}_{12}\text{:Ce}^{3+}$ ,  $\text{Ln}^{3+}$  ( $\text{Ln} = \text{Tb}, \text{Pr}$ ) prepared by polymer-assisted sol-gel method. *J. Lumin.* **132**(11), 3004–3009 (2012).
40. Del Rosario, G., Ohara, S., Mancic, L. & Milosevic, O. Characterisation of YAG:Ce powders thermal treated at different temperatures. *Appl. Surf. Sci.* **238**(1–4), 469–474 (2004).
41. Dorenbos, P. 5d-level energies of  $\text{Ce}^{3+}$  and the crystalline environment. IV. Aluminates and “simple” oxides. *J. Lumin.* **99**(3), 283–299 (2002).
42. Heikkinen, H., Johansson, L.-S., Nykänen, E. & Niinistö, L. An XPS study of SrS:Ce thin films for electroluminescent devices. *Appl. Surf. Sci.* **133**(3), 205–212 (1998).
43. Pfau, A. & Schierbaum, K. D. The electronic structure of stoichiometric and reduced  $\text{CeO}_2$  surfaces: an XPS, UPS and HREELS study. *Surf. Sci.* **321**(1–2), 71–80 (1994).
44. Mullins, D. R., Overbury, S. H. & Huntley, D. R. Electron spectroscopy of single crystal and polycrystalline cerium oxide surfaces. *Surf. Sci.* **409**(2), 307–319 (1998).
45. Zhou, Y. H. *et al.* Morphology control and luminescence properties of YAG:Eu phosphors prepared by spray pyrolysis. *Mater. Res. Bull.* **38**(8), 1289–1299 (2003).
46. Hsu, W. T., Wu, W. H. & Lu, C. H. Synthesis and luminescent properties of nano-sized  $\text{Y}_3\text{Al}_5\text{O}_{12}\text{:Eu}^{3+}$  phosphors. *Mater. Sci. Engin. B-Solid Stat. Mater. Adv. Technol.* **104**(1–2), 40–44 (2003).
47. Han, T. *et al.* Effects of annealing temperature on YAG:Ce synthesized by spray-drying method. *Optik Inter. J. Light. Elect. Opt.* **124**(18), 3539–3541 (2013).

48. Jacobs, R. R., Krupke, W. F. & Weber, M. J. Measurement of excited-state-absorption loss for  $\text{Ce}^{3+}$  in  $\text{Y}_3\text{Al}_5\text{O}_{12}$  and implications for tunable  $5d \rightarrow 4f$  rare-earth lasers. *Appl. Phys. Lett.* **33**(5), 410–412 (1978).
49. Potdevin, A., Chadeyron, G., Boyer, D. & Mahiou, R. Sol-gel based  $\text{YAG}:\text{Ce}^{3+}$  powders for applications in LED devices. *Phys. Stat. Solid. (C)* **4**(1), 65–69 (2007).
50. Zhang, S. *et al.* Long-lasting phosphorescence study on  $\text{Y}_3\text{Al}_5\text{O}_{12}$  doped with different concentrations of  $\text{Ce}^{3+}$ . *J. Rare Earth* **29**(5), 426–430 (2011).
51. Shao, G., Lou, C. & Xiao, D. Enhancing the efficiency of solar cells by down shifting  $\text{YAG}:\text{Ce}^{3+}$  phosphors. *J. Lumin.* **157**(0), 344–348 (2015).
52. Zych, E., Brecher, C. & Glodo, J. Kinetics of cerium emission in a  $\text{YAG}:\text{Ce}$  single crystal: the role of traps. *J. Phys. Condens. Matter.* **12**(8), 1947 (2000).
53. Yang, H. J. *et al.* Facile preparation of  $\text{Y}_{2.9}\text{Ce}_{0.1}\text{Al}_5\text{O}_{12}$  nano-phosphors without photobleaching behavior. *Mater. Lett.* **92**(0), 161–164 (2013).
54. Dong, J., Rapaport, A., Bass, M., Szpocs, F. & Ueda, K.-i. Temperature-dependent stimulated emission cross section and concentration quenching in highly doped  $\text{Nd}^{3+}:\text{YAG}$  crystals. *Phys. Stat. Solid. (A)* **202**(13), 2565–2573 (2005).
55. Chewpraditkul, W. *et al.* Comparative studies of  $\text{Lu}_3\text{Al}_5\text{O}_{12}:\text{Ce}$  and  $\text{Y}_3\text{Al}_5\text{O}_{12}:\text{Ce}$  scintillators for gamma-ray detection. *Phys. Stat. Solid. (A)* **206**(11), 2599–2605 (2009).
56. Zhang, K., Hu, W., Wu, Y. & Liu, H. Photoluminescence investigations of  $(\text{Y}_{1-x}\text{Ln}_x)_3\text{Al}_5\text{O}_{12}:\text{Ce}$  ( $\text{Ln}^{3+} = \text{Gd}^{3+}, \text{La}^{3+}$ ) nanoposphors. *Phys. B: Cond. Matter.* **403**(10–11), 1678–1681 (2008).
57. Blazek, K. *et al.* Luminescence and defects creation in  $\text{Ce}^{3+}$ -doped  $\text{Lu}_3\text{Al}_5\text{O}_{12}$  crystals. *Phys. Stat. Solid. (B)* **241**(5), 1134–1140 (2004).

## Acknowledgements

This work was supported by the National Natural Science Foundation of China (Grant No. 51171007, 51271009 and 61227902).

## Author Contributions

All the authors contributed to the realization of the work and to drafting the manuscript. Prof. R.-H.Y., Dr. X.-F.L. and Dr. student X.-W.H. put forward the original ideas on the explanation of the relationship between local structure and luminescence properties, jointly supervised the work and conceived experiments. Dr. student X.-W.H. finished the IR, NMR, SEM, TEM characterizations and collected the PLE-PL and FLS spectra. Dr. B.Y. measured and explained the TGA-DSC profiles. Dr. student X.-W.H. and R.-F.L. measured and analyzed the XRD patterns, Dr. student X.-W.H. and master student K.-L.Y. synthesized samples. M.Z. acquired the data experiment of XPS. Each of authors has made an indispensable contribution to different aspects of this work.

## Additional Information

**Supplementary information** accompanies this paper at <http://www.nature.com/srep>

**Competing financial interests:** The authors declare no competing financial interests.

**How to cite this article:** He, X. *et al.* Effects of local structure of  $\text{Ce}^{3+}$  ions on luminescent properties of  $\text{Y}_3\text{Al}_5\text{O}_{12}:\text{Ce}$  nanoparticles. *Sci. Rep.* **6**, 22238; doi: 10.1038/srep22238 (2016).



This work is licensed under a Creative Commons Attribution 4.0 International License. The images or other third party material in this article are included in the article's Creative Commons license, unless indicated otherwise in the credit line; if the material is not included under the Creative Commons license, users will need to obtain permission from the license holder to reproduce the material. To view a copy of this license, visit <http://creativecommons.org/licenses/by/4.0/>

Copyright of Scientific Reports is the property of Nature Publishing Group and its content may not be copied or emailed to multiple sites or posted to a listserv without the copyright holder's express written permission. However, users may print, download, or email articles for individual use.